Ultrasonics Sonochemistry 112 (2025) 107168

Contents lists available at ScienceDirect

Ultrasonics Sonochemistry

journal homepage: www.elsevier.com/locate/ultson

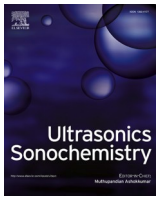

# Experimental and numerical research on jet dynamics of cavitation bubble near dual particles

Yuning Zhang [a], Xuan Lu [a], Jinsen Hu [b], Jiaxin Yu [b,*], Yuning Zhang [b,*]

[a] College of Mechanical and Transportation Engineering, China University of Petroleum-Beijing, Beijing 102249, China
[b] School of Energy Power and Mechanical Engineering, North China Electric Power University, Beijing 102206, China

ARTICLE INFO

*Keywords:*
Cavitation bubble
Jet dynamics
High-speed photography
Numerical simulation
Pressure gradient

ABSTRACT

The current paper delves into the jet dynamics arising from a cavitation bubble in proximity to a dual-particle system, employing both experimental methodology and numerical simulation. The morphological development of a laser-induced bubble as well as the production of jets are captured by utilizing high-speed photography. The principles of bubble morphology evolution and jet formation are revealed by a OpenFOAM solver, which takes into account the effects of two-phase fluid compressibility, phase changes, heat transfer, and surface tension. Fluid temperature variations induced by bubble oscillations are discussed. The results indicate that the jet dynamics can be categorized into three cases, i.e. bubble-splitting double jets, impacting single jet, non-impacting double jets. For bubble-splitting double jets, bubble splitting is induced by an annular pressure gradient towards the bubble axis. This resulted in the production of two unequal-sized sub-bubbles, which subsequently produced double jets in opposite directions. The fluid temperature close to the bubble interface is low, while the bubble center is high. For impacting single jet, it is induced by a conical pressure gradient towards the nearest particle and the jet impacts the particle. The fluid temperature is low near the jet and high near the particle. When the jet penetrates the bubble interface, the temperature inside the bubble reaches its peak. For non-impacting double jets, they are induced by pressure gradients facing each other and they do not impact particles. The temperature inside the bubble increases with the proximity of the two jets.

## 1. Introduction

In the sand-laden rivers, the overflow components of hydraulic machinery are subjected to the combined actions of sand particles and cavitation bubbles within the low-pressure regions [1–3]. The jets formed by cavitation bubbles in proximity to particle clusters are the main factors causing the damage to hydraulic machinery components [4,5]. To mitigate and prevent material damage to these components, it is essential to investigate the formation and the evolution mechanisms of bubble jets in the vicinity of particle clusters. Therefore, the jet dynamics arising from a cavitation bubble collapsing in proximity to particle clusters (namely, a dual-particle system) is investigated through experiments and numerical simulations.

Studies of bubble–particle clusters interactions have focused on bubble morphology evolution, jet characteristics and particle motion characteristics, as shown in Table 1. Exploring the formation and evolution of bubble in proximity to a single particle is the starting point for investigating the bubble near particle clusters. In terms of bubble morphology evolution, Zhang et al. [6] explored the collapsing process of a bubble in proximity to a single particle. They categorized the bubble-collapse morphologies into three cases and correlated these with the bubble–particle distance. To be specific, mushroom, pear, and spherical bubble morphologies were found to correspond to short, medium, and long bubble–particle distances, respectively. Xu et al [7] thoroughly investigated the variation of bubble collapse direction with bubble–particle distance. Their findings reveal that with an increment of bubble–particle distance, the bubble switches from collapsing toward the particle to a centripetal collapse. Wang et al. [8] conducted experimental explorations of bubble morphologies in the vicinity of a particle, with a particular focus on the second period of bubble oscillations. With an increment of bubble–particle distance, the bubble was observed to exhibit three behaviors, namely producing a bulge on the side far from the particle, producing a bulge on the side close to the particle, and splitting into two bubbles.

For bubble jet characterization in proximity to a single particle, Dai et al. [9] evaluated the variation of jet velocity with bubble–particle

* Corresponding authors.
*E-mail addresses:* yujiaxin1012@foxmail.com (J. Yu), yuning.zhang@foxmail.com (Y. Zhang).

https://doi.org/10.1016/j.ultsonch.2024.107168
Received 6 October 2024; Received in revised form 3 November 2024; Accepted 17 November 2024
Available online 19 November 2024

**Table 1**
Current status of research on bubble–particle clusters interaction.

| Object | Physical phenomenon | Refs. |
|---|---|---|
| Single particle | Bubble morphology | 6–8 |
| | Jets | 9–11,14–15 |
| | Particle motion | 16–21 |
| Dual particles | Bubble collapse and particle motion | 22 |
| | Bubble morphology and jet | 23–24 |

distance. Over a wide range of bubble–particle distances, the variations in jet velocity with time show three phases: a slow rise, a sharp rise, and a sharp decline. Zevnik and Dular [10] found that bubble–particle interactions are affected by bubble–particle distance and particle radius. With the distance reduces or the radius increments, the shear stress and the pressure on the particle surface as well as the maximum jet velocity all increase. Li et al. [11] compared the effects of suspended and stationary particle on jet characteristics. Their findings revealed that the jet velocity in proximity to a suspended particle is notably higher than that observed near a fixed particle, yet the Kelvin impulse [12,13] stays at a low value. Moreover, Li et al. [11] found that when the bubble–particle radius ratio is less than 2, a transition occurs as the bubble–particle distance increases. Specifically, at short distances, a single jet directed towards the particle is observed, whereas at long distances, two jets facing each other emerge. Furthermore, for the scenario of two jets, their intensity or velocity is determined by both the bubble–particle distance and the bubble–particle radius ratio. For large bubble–particle radius ratios and small density particles, the results show that the bubble produces a single jet away from the particle when the short bubble–particle distance [14]. Zou et al. [15] analyzed the stratification characteristics of bubble-collapse shock waves near a particle of different shapes, and provided critical conditions for identifying shock wave stratification. Their results reveal that spherically collapsed cavitation bubble produces a monolayer shock wave (i.e., one shock wave), and non-spherically collapsed cavitation bubble results in the stratification of the shock wave (i.e., multiple shock waves).

Characteristics of particle movement driven by cavitation bubble oscillations have received attention. Poulain et al. [16] observed distinct phases in the motion of a particle driven by cavitation bubble, including the bubble's growth pushing the particle away, its collapse drawing the particle closer, and subsequent post-collapse motion towards the bubble, attributed to asymmetric cavitation evolution. Wu et al. [17] further examined the motion of a freely settling particle in the vicinity of a cavitation bubble, documenting four distinct behaviors and developing a force balance model to a elucidate these interactions. Zheng et al. [18] numerically investigated the interactions between a movable particle and a bubble, emphasizing the influence of the particle on the bubble's collapsing shape and the subsequent particle motion triggered by the collapse. Wang et al. [19] delved into the propulsion of a particle from an attached acoustic bubble under the action of strong ultrasonic wave. The direction, amplitude and frequency of ultrasound were found to affect the particle movement characteristics. Xu et al. [20] found that the particle attached to the bubble has various motion modes, such as translation, rotation, posture change and circular motion. The force generated by the expansion and contraction of the bubble pushes the particle to move. The direction of movement is linked to the propagation direction of the radiation force generated by the bubbles, and is closely tied to the position and the shape of the particle. Shen et al. [21] analyzed the displacement, velocity and acceleration characteristics of particles based on experimental and numerical simulation results. They determined that the particle is mainly subjected to the radiative, drag and virtual mass forces of the bubble.

Recently, the phenomenon of cavitation bubble interactions with dual particles has garnered significant attention. Chen et al. [22] experimentally evaluated the interactions of suspended dual particles with a bubble. Their results show that the displacement of the particles is minimal within the first period of the bubble. Zheng et al. [23] researched the morphology of a bubble located in the middle of a dual-particle system. As the bubble–particle distance enlarges, the bubble exhibits four distinct morphologies, namely a gyro-shape, drum-shape, olive-shape, and spherical shape. Hu et al. [24] studied the jet behavior of a bubble positioned centrally between two particles of same radius. Their research revealed that the bubble typically undergoes splitting, resulting in the formation of multiple pairs of jets. Each pair of these jets exhibits the same velocity but travels in opposite directions. However, the precise impact of varying bubble–particle distances on jet characteristics remains an area of uncertainty that warrants further

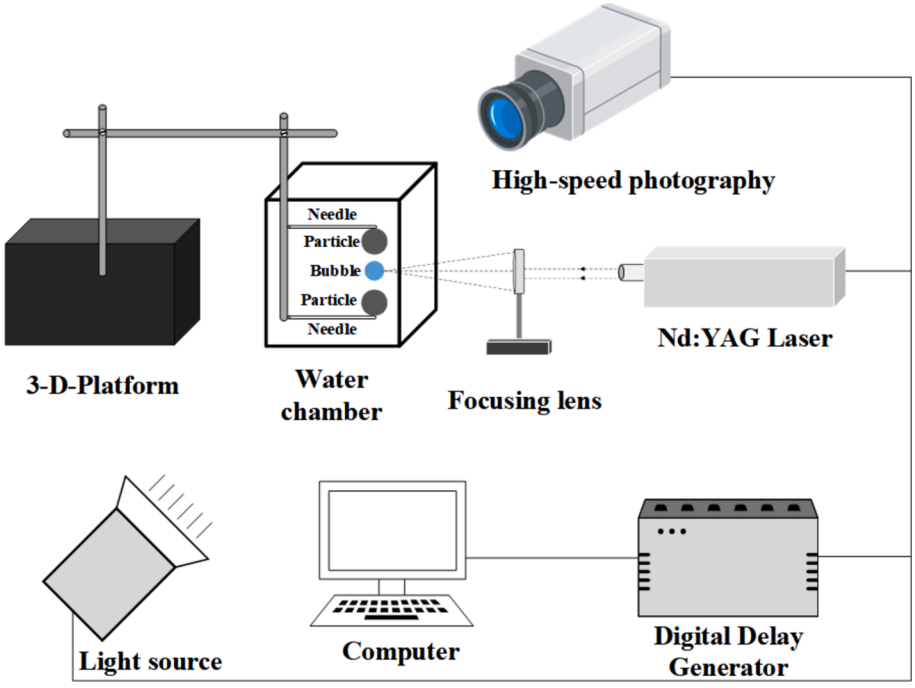


**Fig. 1.** Diagram of the experimental equipment arrangement.

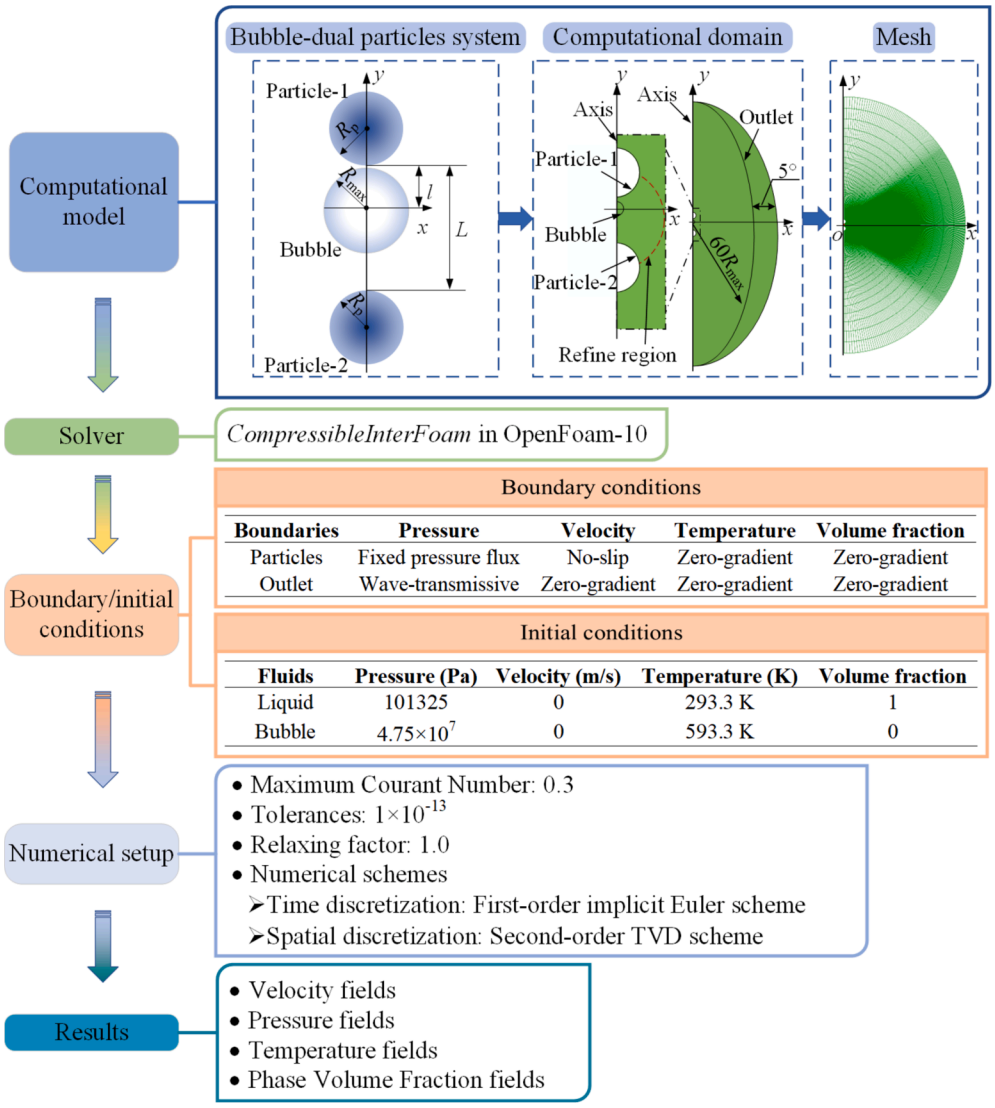


**Fig. 2.** Steps for simulating bubble oscillations.

investigation.

This paper offers a comprehensive exploration of the jet dynamics arising from the cavitation bubble collapsing in proximity to dual particles. Compared with previous studies, this paper obtains the variation rule of jet dynamics with the distance between the bubble and the two particles, as well as the variation rule of the fluid temperature distribution corresponding to each jet behavior. The structure of the subsequent sections is as follows. Section 2 describes the experimental platform for high-speed camera to record bubble morphology. Section 3 outlines the numerical approach utilized to model the bubble near dual particles. Section 4 validates the numerical approach against the results from laser-induced bubble experiments. Section 5 describes three typical jet dynamics produced by a collapsing bubble based on experimental and simulated results. Section 6 discusses the variation of bubble morphology with bubble–particle distance through the velocity–pressure field surrounding the bubble. Section 7 explores the jet velocity variations. Section 8 provides a summary of the key findings and the conclusions of the present work.

## 2. Experimental system for bubble near dual particles

Fig. 1 presents the layout of the experimental equipment. The cavitation bubble is created through focusing the laser beam on deionized water [25]. The experimental procedure is briefly described as follows:

1. Pour deionized water into the water chamber.
2. Turn on the light sources.
3. Identify the precise location at which the bubble will be generated.
4. Glue the $SiO_2$ particles to the needles, which are firmly fixed to the rods 3-D platform.
5. Adjust the spacing between the particles and their positions relative to the bubble using the 3-D platform.
6. Activates the digital delay generator (ZKG027, Minimum adjustment step: 0.15 ns) to send signals to the Nd:YAG laser generator (penny-100-S), light source (BKC-SGW07), and high-speed photography (phantom v1212). The Nd:YAG laser generator emits a laser beam, which passes through the focusing lens (LMH-10X-532) and generates a bubble in deionized water. The light source flashes and illuminates the area around the bubble. The high-speed morphology records pictures of the bubble morphology and stores them in the computer.
7. Repeat steps 5–6 to capture multiple sets of experimental data.

The shooting speed of the high-speed camera is 100,000 fps (frames per second) and the frame size is 256 × 256 pix. The wavelength of the laser generator is 532 nm, the energy is 30mJ and the pulse width is 6 ns.

**Table 2**
Numerical parameters utilized in modeling the liquid and the vapor phase.

| Symbolic | Definition | Value | Unit |
|---|---|---|---|
| $c$ | Compressive parameter | 1 | – |
| $C_{p,l}$ | Specific heat capacity of liquid | 4181.09 | J/(kg·K) |
| $C_{p,v}$ | Specific heat capacity of vapor | 1847.00 | J/(kg·K) |
| $\boldsymbol{F}_s$ | Surface tension force | – | N |
| $I$ | Unit tensor | – | – |
| $K$ | Kinematic energy | – | J |
| $K_c$ | Liquid constant | 472.26 | J/(kg·K) |
| $p$ | Pressure | – | Pa |
| $P_c$ | Pressure constant | $1944.61 \times 10^3$ | Pa |
| $R_v$ | Vapor constant | 461.50 | J/(kg·K) |
| $T$ | Temperature | – | K |
| $T_c$ | Temperature constant | 3837.00 | K |
| $\boldsymbol{U}$ | Velocity | – | m/s |
| $\alpha_l$ | Liquid volume fraction | 1 | – |
| $\alpha_v$ | Vapor volume fraction | 0 | – |
| $\lambda_v$ | Thermal conductivity of vapor | 0.02 | W/(m·K) |
| $\lambda_l$ | Thermal conductivity of liquid | 0.667 | W/(m·K) |
| $\mu$ | Dynamic viscosity | – | Pa·s |
| $\mu_v$ | Dynamic viscosity of vapor | $1.34 \times 10^{-5}$ | Pa·s |
| $\mu_l$ | Dynamic viscosity of liquid | $1.01 \times 10^{-3}$ | Pa·s |
| $\sigma$ | Surface tension coefficient | 0.072 | N/m |
| $\boldsymbol{\tau}$ | Viscous stress tensor | – | Pa |

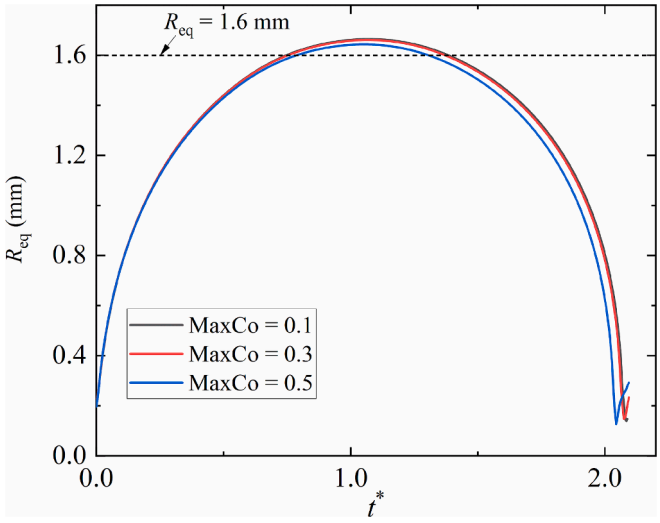


**Fig. 3.** Impact of MaxCo on the bubble equivalent radius ($R_{eq}$). $R_{max}$ = 1.60 mm, $\lambda$ = 1.10, and $\gamma$ = 2.41.

The minimum adjustment step of digital delay generator is 0.15 ns. The focal length of the laser focusing lens is 20 mm.

## 3. Numerical approach for simulating the bubble near dual particles

Fig. 2 gives the five primary steps for simulating the bubble behaviors in bubble–particle system. In preparing the computational model, the bubble–dual particles system shows an arrangement of a bubble and two particles, together with the key parameters. To facilitate understanding and analysis, the following dimensionless parameters are defined as

$$\lambda = \frac{l}{R_{max}}, \tag{1}$$

$$\gamma = \frac{L}{R_{max}}, \tag{2}$$

$$t^* = \frac{t}{t_c}, \tag{3}$$

where $R_{max}$ represents the maximum bubble radius. $t_c = R_{max}\sqrt{\rho_{l,\infty}/p_\infty}$ is the Rayleigh collapse time [26]. $p_\infty$ is the ambient pressure, which is set to 101325 Pa. $\rho_{l,\infty}$ denotes the density of the liquid at infinity, specified as 997.0 kg/m$^3$. $t$ signifies the time. In this paper, both particles have the same radius of 1.5 mm.

Since the bubble–dual particles system is symmetric about the $y$-axis, an axisymmetric computational region is adopted to minimize the computational cost while maintaining accuracy. The computational field size is set to $60R_{max}$. A $4R_{max}$ region (red dotted line) near the bubble and particles is refined in order to ensure accurate acquisition of the bubble interface.

The compressibleInterFoam solver in OpenFOAM-10 [27] is used to obtain solutions. Using volume of fluid approach to accurately trace bubble interfaces [28]. The solver treats the fluid properties and the momentum as a "mixture" and solves a single momentum equation [29]. During bubble collapse, phase change occurs proximate to the bubble interface, driven by pressure gradients and temperature variations [30]. Therefore, the solver considers the temperature transfer and the phase change. Due to the cavitation bubble studied in this paper is millimeter scale, the buoyancy parameter$\delta = \sqrt{\rho_l g R_{max}/p_\infty} = 0.012$, suggests that the effect of buoyancy on jet formation can be neglected [31].

The fluid equations are now described in detail. The continuity equations for two phases are

$$\frac{\partial \alpha_l \rho_l}{\partial t} + \nabla \bullet (\alpha_l \rho_l \boldsymbol{U}) = +\dot{m}, \tag{4}$$

$$\frac{\partial \alpha_v \rho_v}{\partial t} + \nabla \bullet (\alpha_v \rho_v \boldsymbol{U}) = -\dot{m}, \tag{5}$$

with

$$\rho = \alpha_l \rho_l + \alpha_v \rho_v, \tag{6}$$

where the subscripts "$l$" and "$v$" are used to separate the variables for liquid and vapor. The mass transfer rate $\dot{m}$ is modeled on the basis of a modified Schnerr-Sauer model [32–34].

The momentum, volume fraction, energy and state equations for the two phases are given below [35–39]

$$\frac{\partial \rho \boldsymbol{U}}{\partial t} + \nabla \bullet (\rho \boldsymbol{U}\boldsymbol{U}) = -\nabla p + \nabla \bullet \boldsymbol{\tau} + \boldsymbol{F}_s, \tag{7}$$

$$\begin{aligned} &\frac{\partial \alpha_l}{\partial t} + \nabla \bullet (\alpha_l \boldsymbol{U}) + \nabla \bullet (\alpha_l(1-\alpha_l)\boldsymbol{U}_r) \\ &= \alpha_l \alpha_v \left(\frac{1}{\rho_v}\frac{d\rho_v}{dt} - \frac{1}{\rho_l}\frac{d\rho_l}{dt}\right) + \dot{m}\left[\frac{1}{\rho_l} - \alpha_l\left(\frac{1}{\rho_l} - \frac{1}{\rho_v}\right)\right] + \alpha_l \nabla \bullet \boldsymbol{U} \end{aligned}, \tag{8}$$

$$\begin{aligned} &\frac{\partial \rho T}{\partial t} + \nabla \bullet (\rho \boldsymbol{U} T) + \left(\frac{\alpha_l}{C_{p,l}} + \frac{\alpha_v}{C_{p,v}}\right)\left[\frac{\partial \rho K}{\partial t} + \nabla \bullet (\rho \boldsymbol{U} K)\right] \\ &= \left(\frac{\alpha_l}{C_{p,l}} + \frac{\alpha_v}{C_{p,v}}\right)\left[\frac{\partial p}{\partial t} + \nabla \bullet (\tau \bullet \boldsymbol{U})\right] + \left(\frac{\alpha_l \lambda_l}{C_{p,l}} + \frac{\alpha_v \lambda_v}{C_{p,v}}\right)(\nabla^2 T) \end{aligned} \tag{9}$$

$$\rho_l = \frac{p + p_c}{K_c(T + T_c)}, \tag{10}$$

$$\rho_v = \frac{p}{R_v T}, \tag{11}$$

with

$$\boldsymbol{\tau} = \mu\left[\nabla \boldsymbol{U} + (\nabla \boldsymbol{U})^T - \frac{2}{3}(\nabla \bullet \boldsymbol{U})I\right], \tag{12}$$

$$\mu = \alpha_l \mu_l + \alpha_v \mu_v, \tag{13}$$

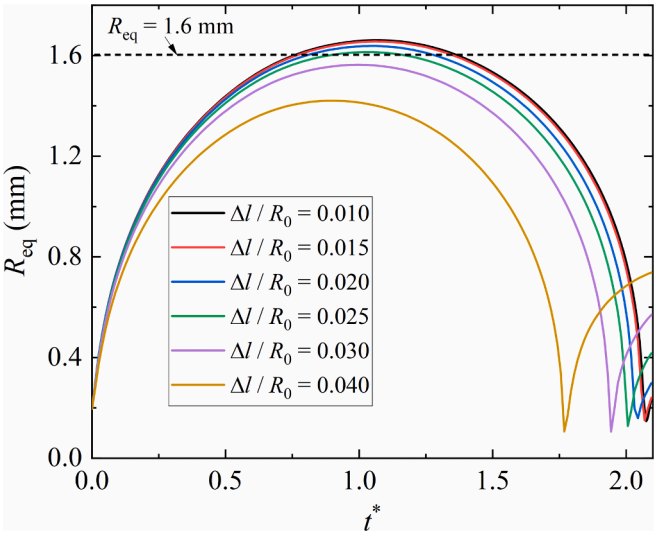


**Fig. 4.** Mesh independence results. $R_{max}$ = 1.60 mm, $\lambda$ = 1.10, and $\gamma$ = 2.41.

$$\boldsymbol{F}_s = \sigma \nabla \bullet \left( \frac{\nabla \alpha_l}{|\alpha_l|} \right) \nabla \alpha_l, \tag{14}$$

$$\boldsymbol{U}_r = c|\boldsymbol{U}| \frac{\nabla \alpha_l}{|\nabla \alpha_l|}. \tag{15}$$

Table 2 gives the definitions of the symbolics in the set of control equations and the values of the key parameters.

In setting the boundary/initial conditions, the particle surfaces are given the wall condition, and the outlet is assigned the non-reflective wave condition [40]. To obtain the morphology of the bubble during its expansion, its initial radius ($R_0$) is given as 0.2 mm. The temperature inside the initial bubble is fixed at 593.3 K and the initial pressure is varied to obtain a bubble with different maximum radii. When the initial pressure is given as 47.5 MPa, the $R_{max}$ of the bubble reaches 1.50 mm. However, if the initial pressure is increased to 56.0 MPa, the bubble grows even further, reaching a maximum radius of 1.60 mm.

In numerical settings, the time step is dynamically varied according to the maximum Courant number (MaxCo) [41]. Fig. 3 demonstrates the maximum Coulomb number on the equivalent radius of the bubble. Here, the equivalent radius ($R_{eq}$) is $\sqrt{A/\pi}$, where $A$ represents the areas of the two-dimensional cross section of the bubble. Due to the extrusion of two particles, the maximum equivalent of the bubble is larger than the maximum radius of the bubble in the absence of particles. The maximum relative errors for MaxCo of 0.5 and 0.3 relative to MaxCo of 0.1 are 3.1 % and 8.3 %, respectively. Consequently, to balance computational efficiency and accuracy, a MaxCo of 0.3 was chosen for this study. The

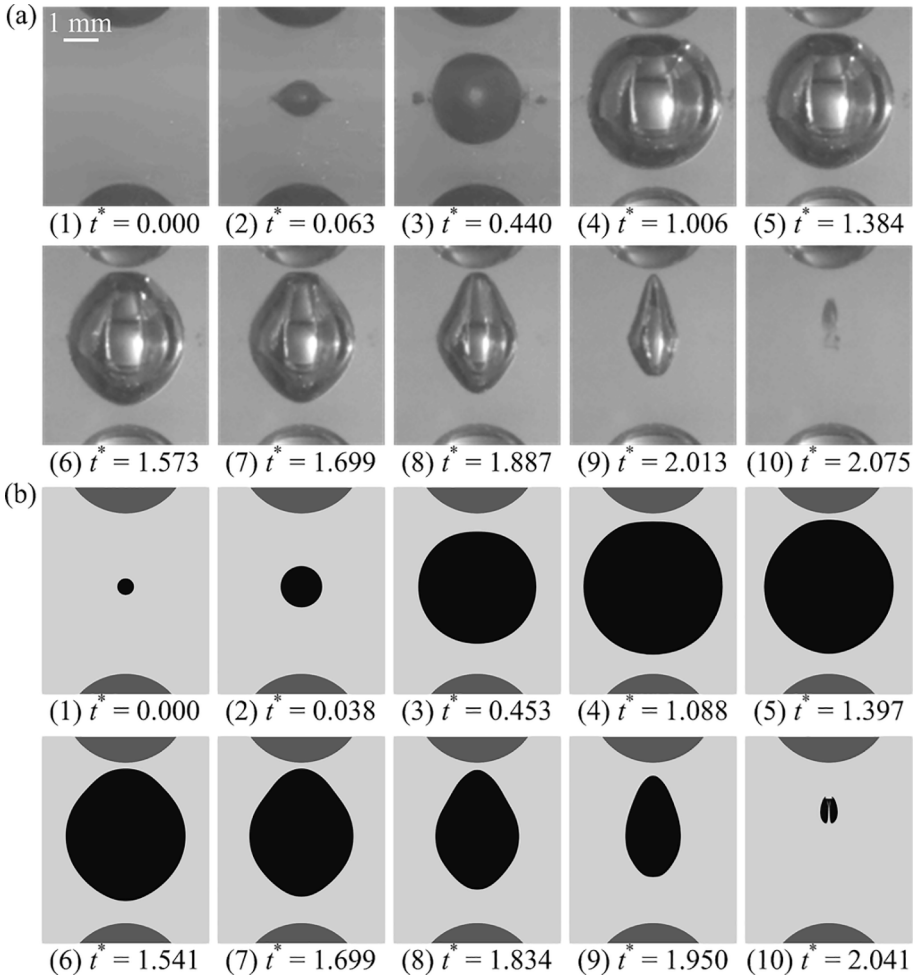


**Fig. 5.** Comparisons of bubble morphology evolution. (a) Experimental results. (b) Numerical results. In the simulation results, black areas correspond to bubbles, gray areas to liquids, and dark gray areas to particles. $R_{max}$ = 1.60 mm, $\lambda$ = 1.10, and $\gamma$ = 2.41.

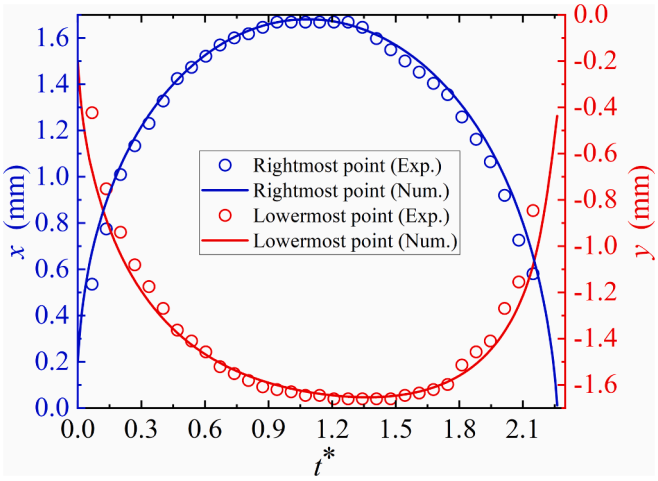


**Fig. 6.** Comparison of experimentally measured displacements and simulated predicted displacements at two feature points. The blue circles/lines indicate the displacement of the rightmost point of the bubble interface. The red circles/lines indicate the displacement of the lowermost point of the bubble interface. $R_{max} = 1.60$ mm, $\lambda = 1.10$, and $\gamma = 2.41$. (For interpretation of the references to colour in this figure legend, the reader is referred to the web version of this article.)

tolerance of the matrix solver is set to $1 \times 10^{-13}$ to minimize the error generated by the iteration of the equations. The time discretization and space discretization are performed using first- and second-order numerical schemes, respectively. Finally, the velocity fields, pressure fields, temperature fields, and phase volume fraction fields generated by bubble oscillations are obtained.

Fig. 4 presents the simulation outcomes of the cavitation bubble at different mesh refinement levels. The mesh refinement parameter $\Delta l$ is the maximum distance between neighboring nodes, as measured along the red dashed line depicted in Fig. 2. When $\Delta l = 0.015R_0$, mesh convergence is achieved. Therefore, to reduce the computational cost, a mesh with a refinement level of 0.015 $R_0$ is selected.

## 4. Experimental validations based on a laser-induced bubble

The morphological variation of the bubble depends on the distance from it to the particle. Therefore, a set of experimental results with a bubble slightly closer to the particle-1 is used to verify the correctness of the numerical solver. Fig. 5 compares the evolution of the bubble morphology in proximity to the dual-particles system given by the experimental and numerical approaches. When the digitizer controls the Nd:YAG laser generator to emit laser light, it also sends a signal to the light source to flash and illuminate the area around the bubble. From the moment the laser is focused until the bubble grows to 20 % of its maximum radius, the intensity of the light source gradually increases to its maximum. In order to clearly demonstrate the bubble morphology, the brightness of frames 1 ~ 2 of Fig. 5(a) was manually increased. In Fig. 5(a) and 5(b), the experimental and simulated bubble morphologies are in good agreement. Fig. 6 compares the experimentally measured displacements of two feature points with those predicted by the simulation. The rightmost and lowermost points of the bubble interface are selected for further comparisons. From Figs. 5 and 6, the numerical model demonstrates a high accuracy in forecasting the experimental bubble morphology evolution.

## 5. Typical jet dynamics produced by the collapsing bubble

### 5.1. Main features of jets

Fig. 7 shows the main features and the classification of the bubble jet in proximity to the dual particles system obtained from the numerical results. Considering that the same radii of the two particles and neglecting the buoyancy effect, the jet behavior when the incipient location of the bubble approaches particle-2 is symmetrical to that when the incipient location of the bubble approaches particle-1. Hence, only the cases in which the bubble is biased toward particle-1 are discussed. According to the count and formation mechanism of jets, three cases of jet dynamics can be distinguished. For the case of bubble-splitting double jets ($\lambda < 1.0$ and $\gamma < 2.0$), the bubble–particle distances are short, and the bubble splits to two differently sized sub-bubbles. After the bubble splits, the double jets moving in opposite directions are created. For the case of impacting single jet ($\lambda < 1.0$ and $\gamma > 2.0$), the bubble approaches one of the particles and produces a single jet, which will impact the nearest particle. For the case of non-impacting double jets ($\lambda > 1.0$ and $\gamma > 2.0$), the bubble–particle distances are large, and the double jets facing each other are produced. Eventually, the two jets collide and the bubble transforms into an annular bubble.

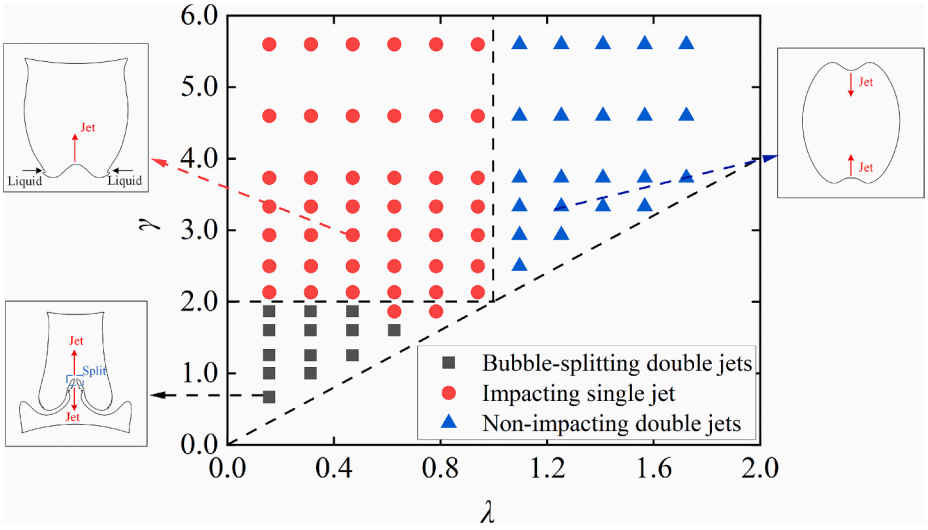


**Fig. 7.** Main features and classifications of the jet dynamics near the dual-particle system. Three black dashed lines serve as the dividing line between the three cases. $R_{max} = 1.50$ mm.

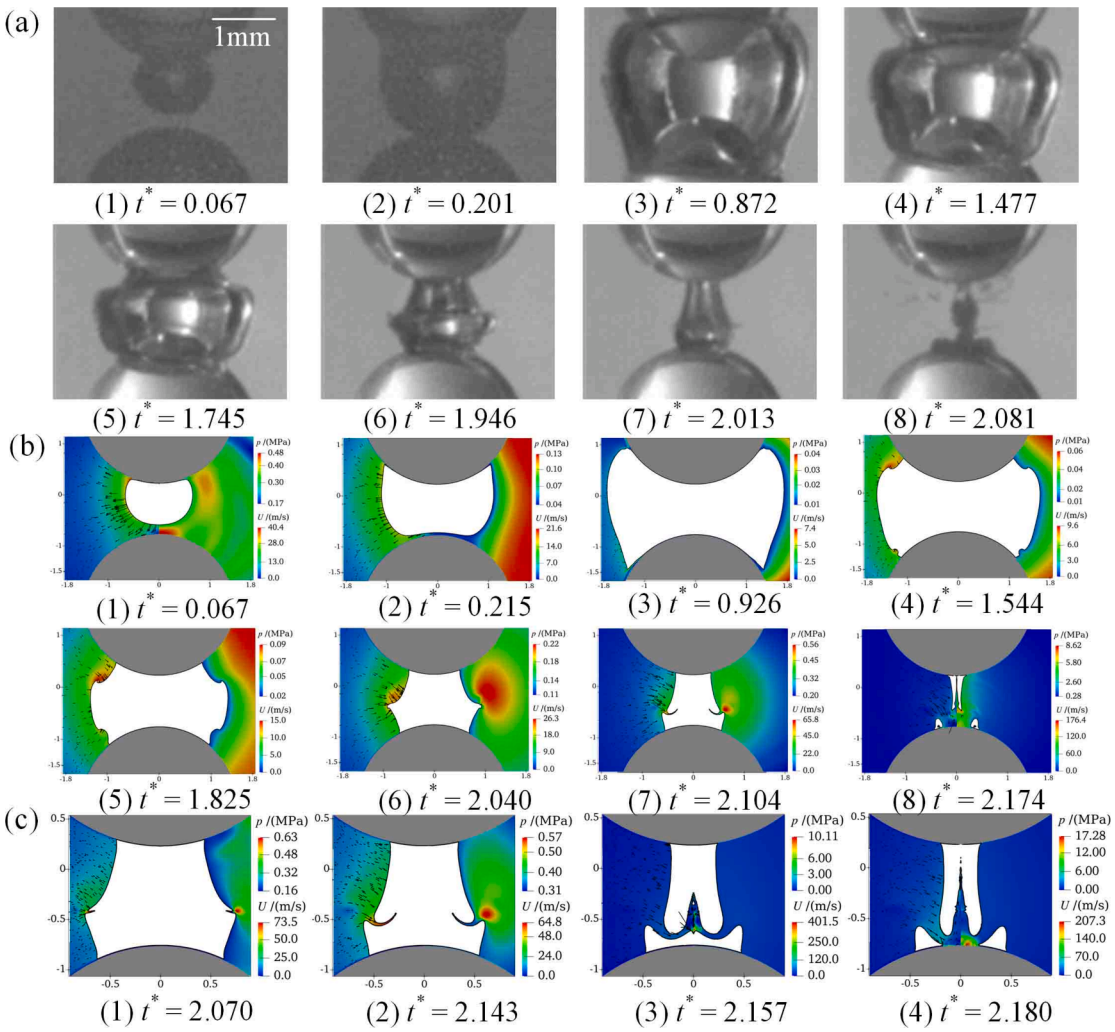


**Fig. 8.** Bubble morphology evolution and jet formation for the case of bubble-splitting double jets. (a) Experimental results. (b) Simulated results. (c) Evolution of the jet. In the simulated results, the left part of each subplot indicates the velocity field, and arrows indicate the velocity vectors. The right part indicates the pressure field. The gray parts indicate the particles. $\lambda = 0.16$, $\gamma = 0.67$, and $R_{max} = 1.50$ mm.

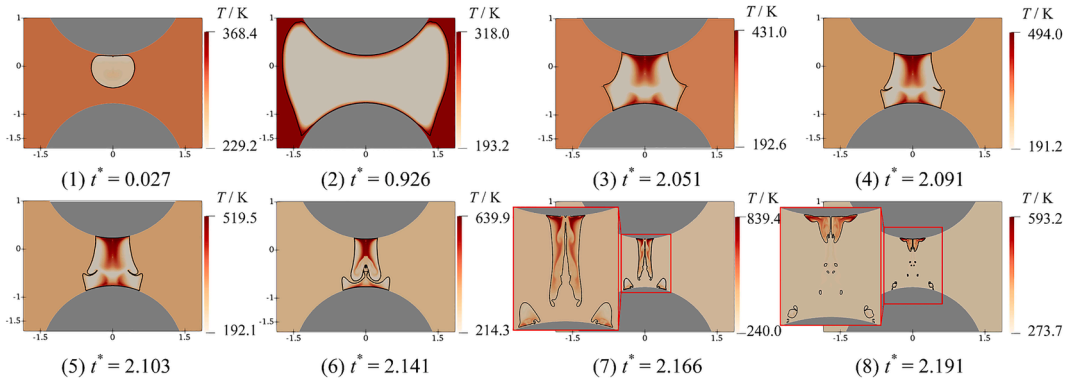


**Fig. 9.** The temperature field evolution surrounding the bubble for the case of bubble-splitting double jets. The solid black lines are the bubble interface. The gray parts indicate the particles. $\lambda = 0.16$, $\gamma = 0.67$, and $R_{max} = 1.50$ mm.

### 5.2. *Bubble-splitting double jets*

Fig. 8 illustrates the bubble morphology evolution and jet formation for the case of bubble-splitting double jets. Fig. 8(a) and 8(b) correspond to the experimental and simulated bubble morphologies, respectively. Fig. 8(c) specifically shows the jet formation. In Fig. 8(a), the small values of $\lambda$ and $\gamma$ bring the cavitation bubble closer to particle-1, initiating contact with it before particle-2. As the bubble expands to its fullest extent shown in frame 3, it partially envelops both particles. Subsequently, in frames 4–6 of Fig. 8(a), the bubble interface close to the two particles shrinks faster than other positions, resulting in the formation of two necks. Finally, as depicted in frames 7–8 of Fig. 8(a), the

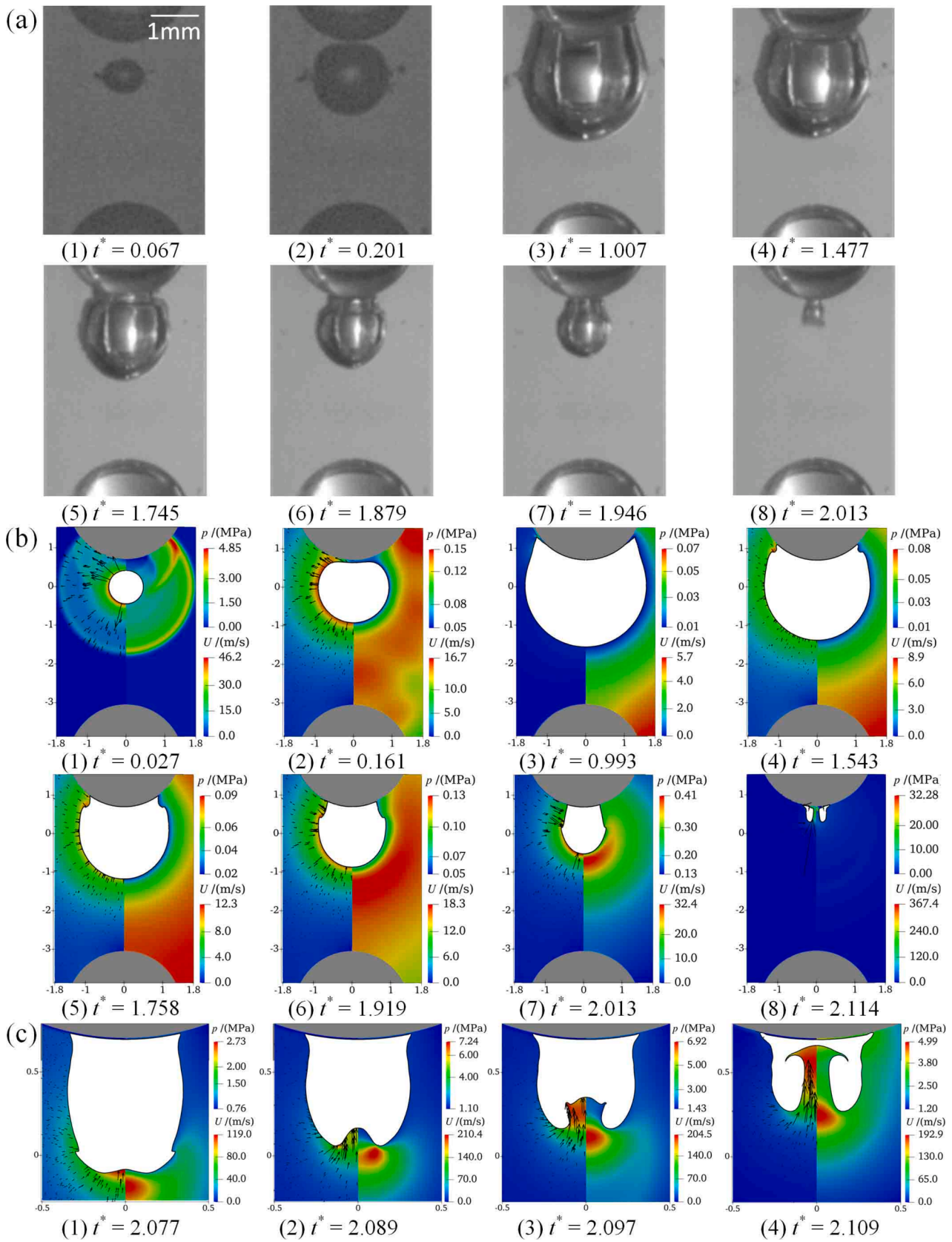


**Fig. 10.** Cavitation bubble morphology evolution and jet formation for the case of impacting single jet. (a) Experimental results. (b) Simulated results. (c) Evolution of the jet. In the simulated results, the left part of each subplot indicates the velocity field, and arrows indicate the velocity vectors. The right part indicates the pressure field. The gray parts indicate the particles. $\lambda = 0.47$, $\gamma = 2.5$, and $R_{max} = 1.50$ mm.

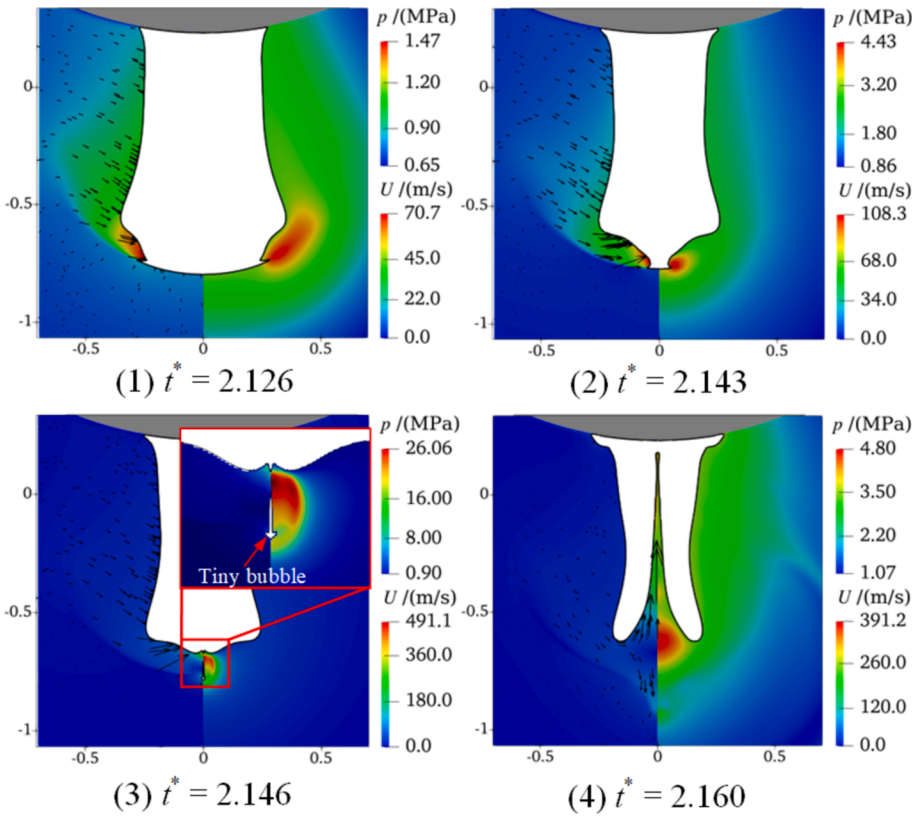


**Fig. 11.** Mechanisms of jet formation for the case of impacting single jet. The left part of each subplot indicates the velocity field, and arrows indicate the velocity vectors. The right part indicates the pressure field. The gray parts indicate the particles. $\lambda = 0.16$, $\gamma = 3.33$, and $R_{max} = 1.50$ mm.

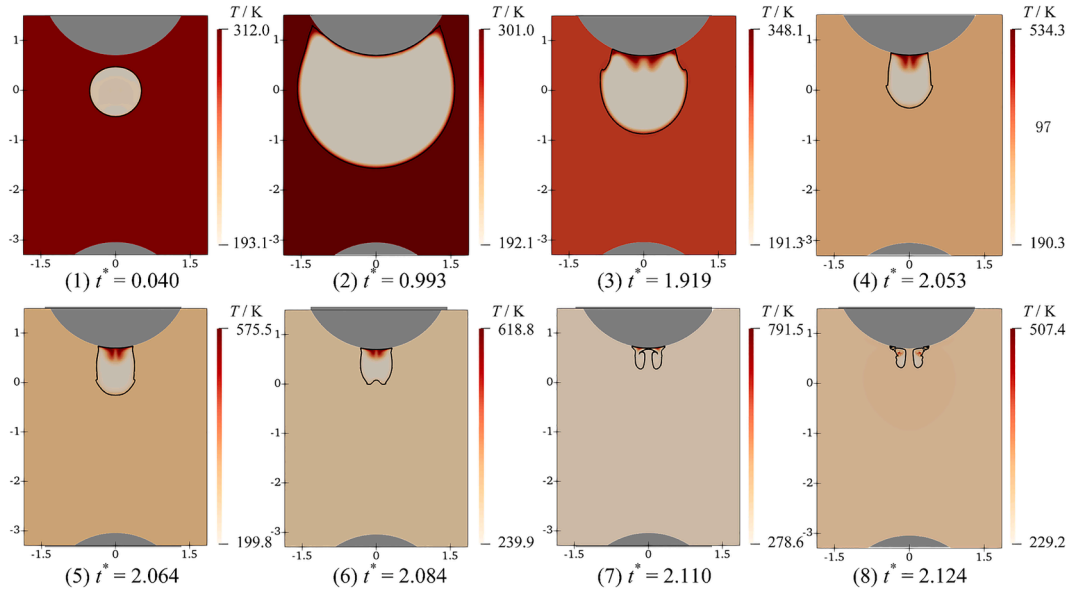


**Fig. 12.** The temperature field evolution surrounding the bubble for the case of impacting single jet. The solid black line is the bubble interface. The gray parts indicate the particles. $\lambda = 0.47$, $\gamma = 2.5$, and $R_{max} = 1.50$ mm.

bubble breaks into two parts, which become attached to the two particles.

In frames 3–4 of Fig. 8(b), the liquid close to the particles generates a concavity in the bubble interface, creating two localized high-pressure regions. These regions lead to the formation of two necks. As shown in frames 5–6 of Fig. 8(b), driven by a pressure gradient, the two necks shrink centripetally along the bubble interface and eventually collide. An annular depression is then generated in the middle of the bubble. The presence of a region of high-pressure gradient adjacent to particle-1 causes the annular depression to draw closer to particle-2. In frames 7–8 of Fig. 8(b), the bubble is split by the annular depression into two sub-bubbles, each of which collapses toward the nearest particle.

In the first frame of Fig. 8(c), when the two necks collide, the bubble produces a narrow annular region. This region is the result of an annular

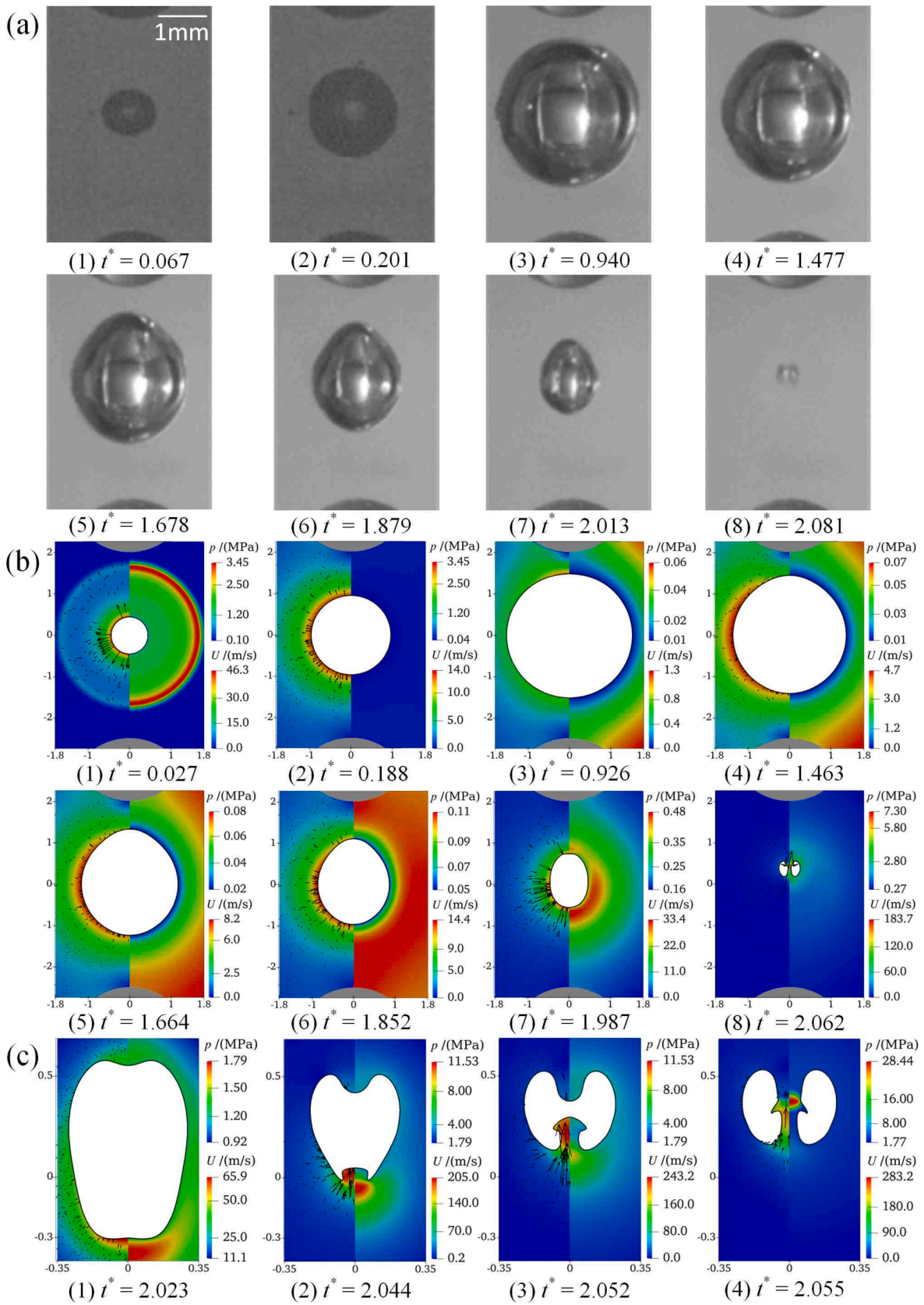


**Fig. 13.** Cavitation bubble morphology evolution and jet formation for the case of non-impacting double jets. (a) Experimental results. (b) Simulated results. (c) Evolution of the jet. In the simulated results, the left part of each subplot indicates the velocity field, and arrows indicate the velocity vectors. The right part indicates the pressure field. The gray parts indicate the particles. $\lambda = 1.34$, $\gamma = 3.00$, and $R_{max} = 1.50$ mm.

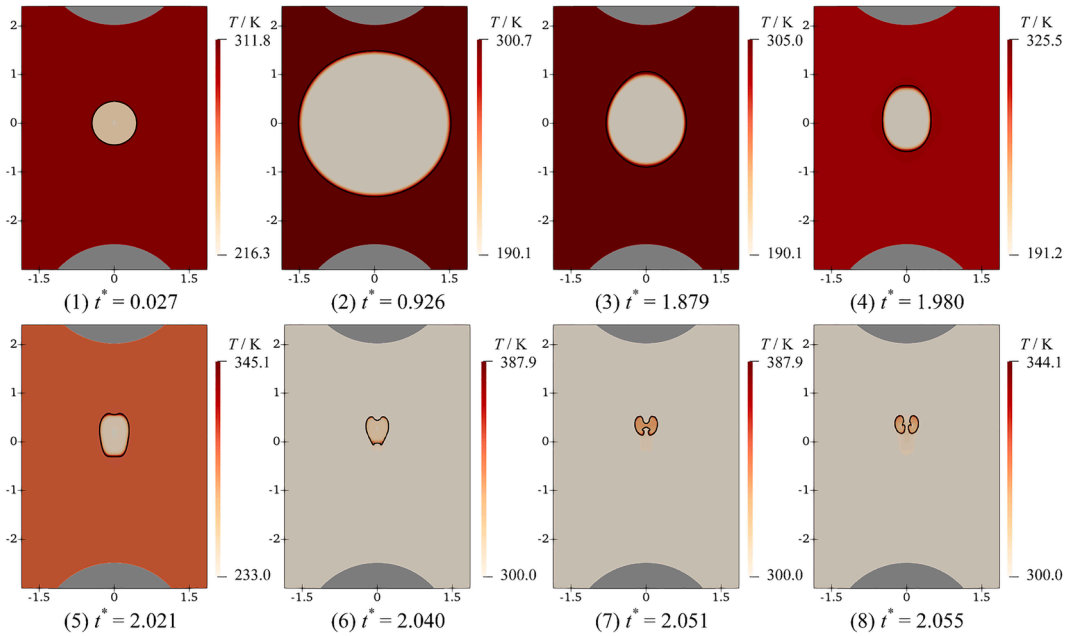


**Fig. 14.** The temperature field evolution surrounding the bubble for the case of non-impacting double jets. The solid black line is the bubble interface. The gray parts indicate the particles. $\lambda = 1.34$, $\gamma = 3.00$, and $R_{max} = 1.50$ mm.

pressure gradient towards the bubble axis acting on the bubble interface. The liquid in this region forces the middle part of the bubble converge towards its axis, which in turn causes the bubble to split. In frame 3 of Fig. 8(c), the pressure gradient at the split point forces both sub-bubbles to produce jets simultaneously. The two jets demonstrate opposite directions. In time, the jet hitting particle-1 inside the upper sub-bubble lags behind the jet impacting particle-2 inside the lower sub-bubble.

Fig. 9 indicates the temperature field evolution surrounding the bubble for the case of bubble-splitting double jets. In frames 1–2, the temperature inside bubble decreases and stays at a low value as the bubble grows. As the bubble collapsing, the phase change begins in the region adjacent to the bubble interfaces [42]. In the region of phase change, the temperature gradient towards the interior of the bubble can be clearly observed. Due to the combined effects of the temperature gradient and the pressure gradient, the vapor within the bubble condenses. During bubble collapse (frames 3–8 in Fig. 9), the temperature proximal to the bubble interface maintains a low level, whereas the temperature in the bubble center escalates, prompting evaporation in this region. As the condensation surpasses the evaporation within the bubble, its mass progressively diminishes. Throughout the evolution of the bubble, its internal temperature changes significantly, while the external temperature changes slowly.

### 5.3. Impacting single jet

Fig. 10 illustrates the bubble morphology evolution and jet formation for the case of impacting single jet. Fig. 10(a) and 10(b) show the experimental and simulated bubble morphologies, respectively. Fig. 10(c) illustrates the jet formation. From frames 3 to 5 of Fig. 10(a), the bubble expands, with its upper part gradually enveloping the lower part of Particle-1 while maintaining a spherical shape at its lower end. As shown in frames 4–8 of Fig. 10(a), a neck forms in the upper part of the bubble, preceding its collapse towards particle-1. In Fig. 10(b), frame 1 presents a pressure wave generated during bubble inception. With the bubble collapses [frames 5–7 in Fig. 10(b)], particle-1 obstructs the shrinkage of the upper part of the bubble, causing the liquid, influenced by a pressure gradient directed towards particle-1, to push the bubble towards it. Comparing the experimental observation [frame 8 of Fig. 10(a)] with the numerical result [frame 8 of Fig. 10(b)], the latter reveals the presence of the toroidal bubble and the jet. In Fig. 10(c), a region of conical pressure gradient towards particle-1 appears below the bubble, which gives rise to the generation of a jet towards particle-1.

Fig. 11 illustrates the mechanism of jet formation for a bubble close to particle-1. Compared with Fig. 10, we can observe a distinct mechanism for jet formation. In frames 1–2, the liquid below the bubble converges to the symmetry axis. Subsequently, a tiny bubble detaches from the main bubble and foams a tiny region with high pressure gradient at the detachment location. Under the influence of the pressure gradient, one jet evolves at the bubble bottom (frame 4). From frames 3 to 4, following the separation of the tiny bubble, the jet displays a narrow diameter and high velocity, referred to as a needle jet. This phenomenon has also been observed in the researches conducted by Lechner et al. [43] and Reuter et al. [44] on jets near flat wall. Compared to the findings of Lechner et al. [43] and Reuter et al. [44], all the needle jets are produced by collisions of bubble interfaces. However, the difference is that the needle jet in this paper is generated at the end of the first period of the bubble.

Fig. 12 presents the temperature field evolution surrounding the bubble for the case of impacting single jet. In frames 3–8, the bubble collapses and high temperature region concentrates inside the bubble approaching particle-1. As the jet moves toward particle-1, the temperature within the bubble rises. Once the jet impinges on the bubble interface (frame 7 of Fig. 12), the local temperature reaches its peak value.

### 5.4. Non-impacting double jets

Fig. 13 illustrates the bubble morphology variation and jet formation for the case of non-impacting double jets. Fig. 13(a) and 13(b) display the experimental and simulated bubble morphologies, respectively. Fig. 13(c) specifically shows the jet evolution. In this case, the distances from the bubble to both particles are long. From first to third frames of Fig. 13(a), in contrast to the two previously mentioned cases, the bubble never contacts the particles and remains approximately spherical. During the collapse stage of bubble [frames 4–7 in Fig. 13(a)], its upper part shrinks significantly, and the bubble becomes egg-shaped. Finally, the bubble collapses centripetally.

In Fig. 13(b), the inhomogeneous distribution of velocity–pressure

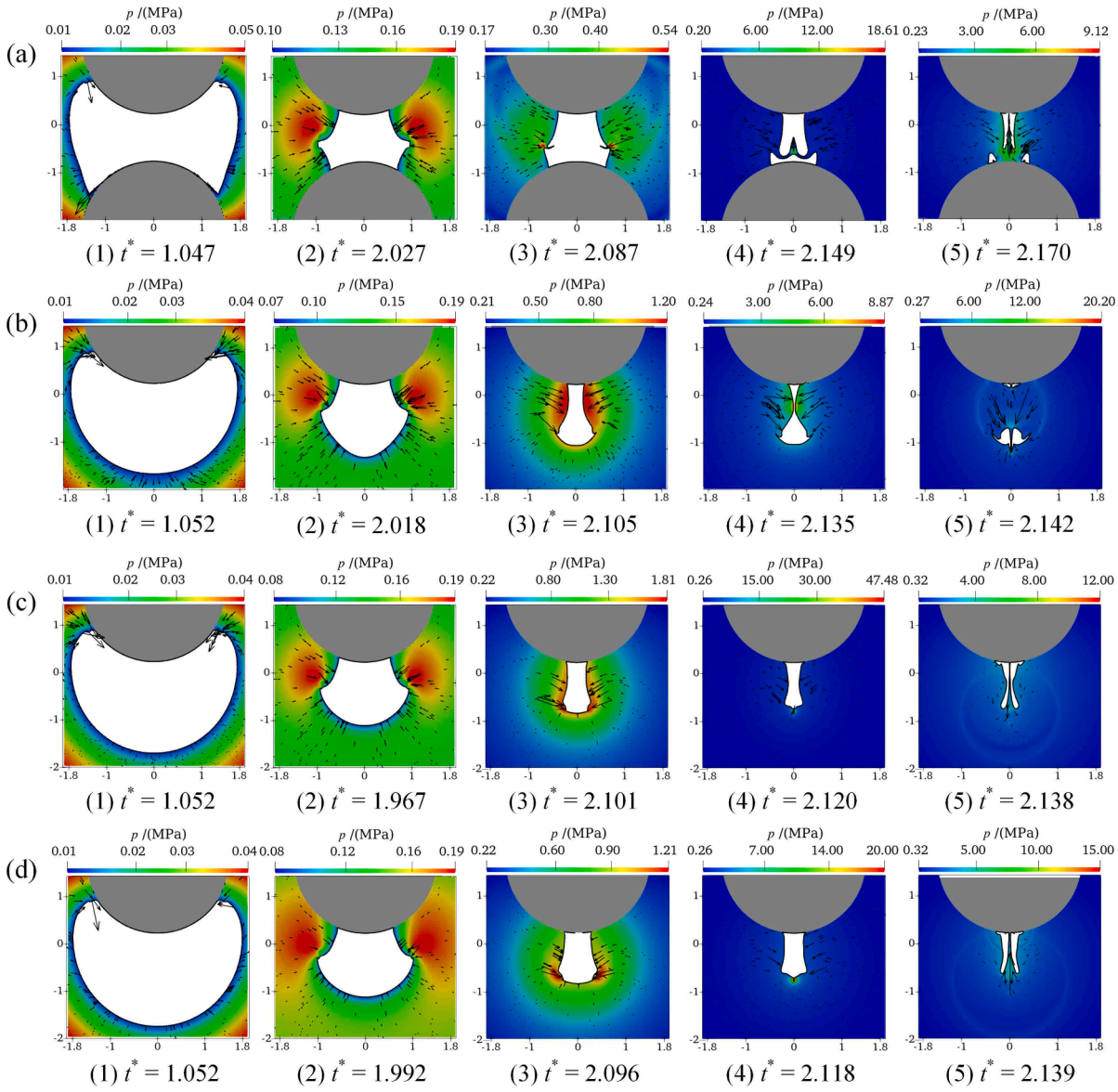


**Fig. 15.** Effect of particle spacing parameter $\gamma$ on the jet behaviour for $\lambda = 0.16$. The arrows represent the velocity vectors. (a) $\gamma = 0.67$. (b) $\gamma = 1.60$. (c) $\gamma = 2.13$. (d) $\gamma = 5.6$. $R_{max} = 1.50$ mm.

field reveals the mechanism of the bubble morphology evolves. As the bubble nears particle-1 in frames 4–8 of Fig. 13(b), a pressure differential arises, with the pressure beneath the bubble exceeding that above it. This gradient intensifies the contraction of the lower part of the bubble.

In Fig. 13(c), the bubble is subjected to two pressure gradients in opposite directions to form the double jets facing each other. Due to the bubble being close to particle-1, the intensity of the pressure gradient below the bubble exceeds the gradient above. The difference in pressure gradient strength leads to the bubble moving towards particle-1 and causes the jet directed towards particle-1 to be rapid. After the two jets collide, the cavitation bubble transforms into an annular bubble. At the same time, the convergence of the two jets creates a localized zone of heightened pressure gradient surrounding the symmetry axis. The liquid in this region turns the axial jets to form radial jets.

Fig. 14 shows the temperature field evolution surrounding the bubble for the case of non-impacting double jets. Prior to jet generation (frames 2–5 in Fig. 14), most of the region within the bubble is cryogenic and condensation is dominant. After the jets are generated (frame 6 in Fig. 14), there is a gradual increase in temperature within the bubble. As the bubble continues to collapse, its interior is occupied by vapor with high temperature and high pressure.

## 6. Effects of bubble–particle distance on jet behaviour

Fig. 15 presents the effect of the particle spacing parameter $\gamma$ on the jet behaviour for same bubble–particle-1 distance ($\lambda = 0.16$). From Fig. 15(a)–15(d), $\gamma$ gradually increments. In Fig. 15(a), the collision of the annular depression reads to the bubble splitting, resulting in the formation of double jets. In Fig. 15(b), an annular high-pressure gradient region near the neck leads to a faster shrinkage in the middle of the bubble than at other positions. Under the influence of the annular pressure gradient, the bubble neck develops towards its axis, leading to bubble splitting. At the same time, two jets moving in opposite directions are formed. Compared with Fig. 15(a) and 15(b), the bubble splits closer to the lower part in Fig. 15(c). The extremely small bubble collapses quickly without generating jets, and the large bubble produces one jet toward particle-1. Fig. 15(d) exhibits jet behavior similar to that of Fig. 15(c).

Fig. 16 shows the impact of the particle spacing parameter $\gamma$ on the

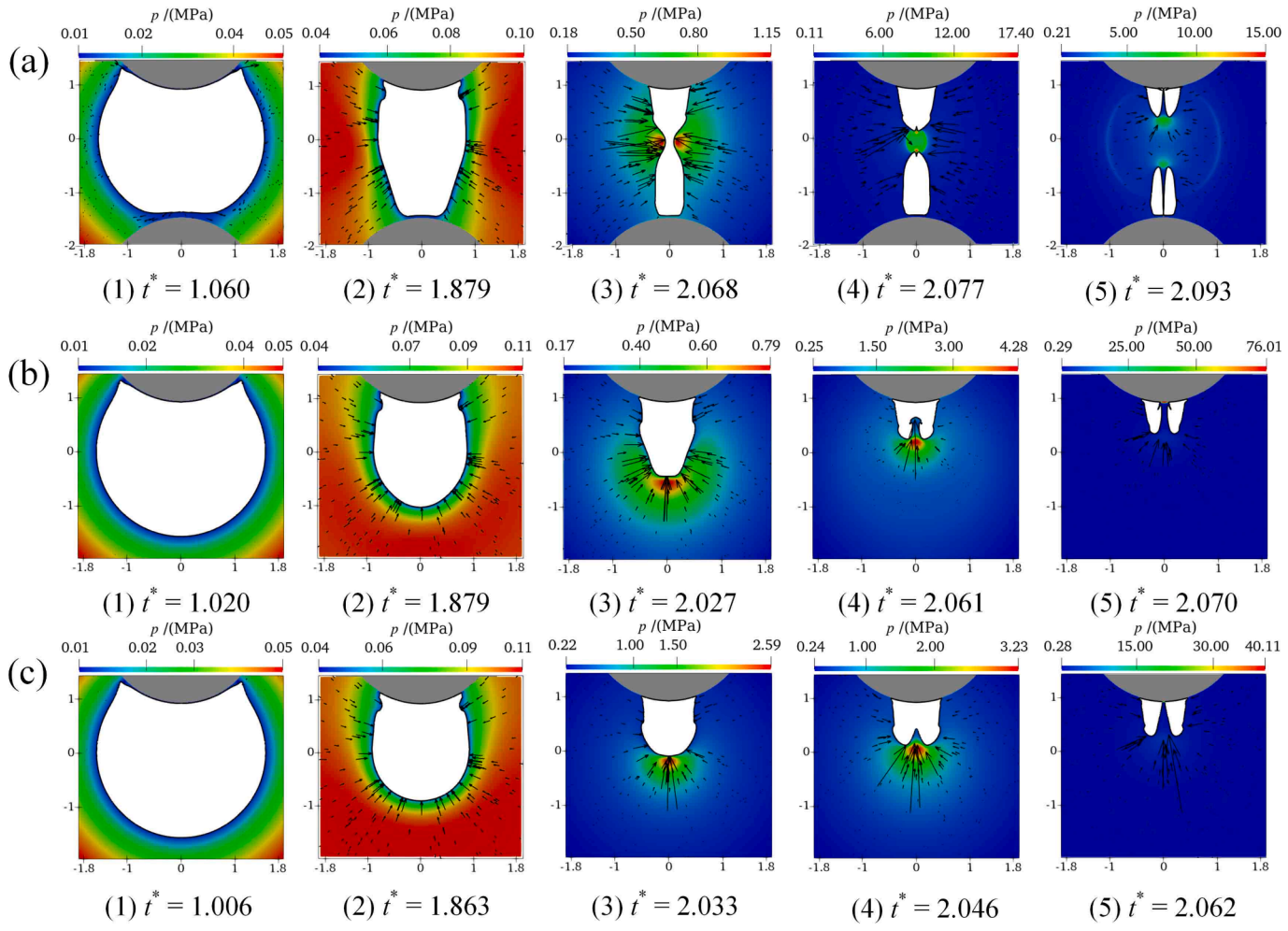


**Fig. 16.** Effect of particle spacing parameter $\gamma$ on the jet behaviour for $\lambda = 0.63$. The arrows represent the velocity vectors. (a) $\gamma = 1.60$. (b) $\gamma = 2.13$. (c) $\gamma = 5.60$. $R_{max} = 1.50$ mm.

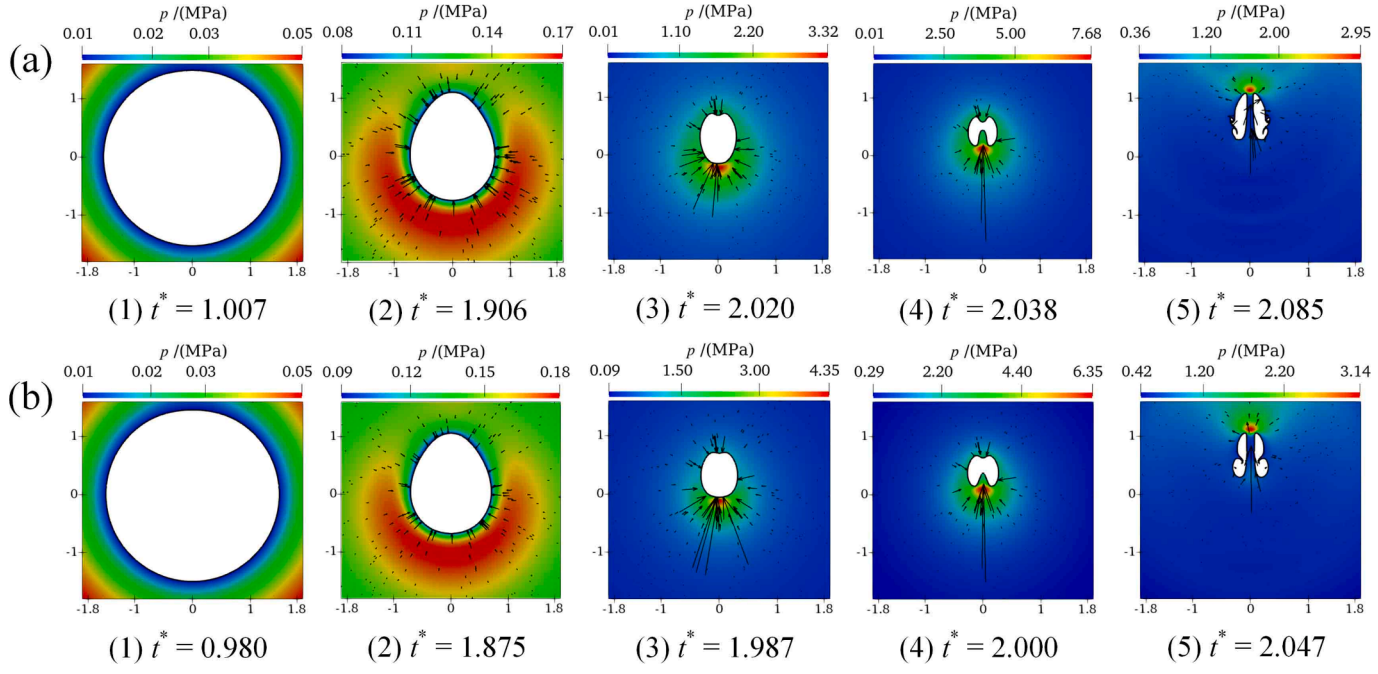


**Fig. 17.** Effect of particle spacing parameter $\gamma$ on the jet behaviour for $\lambda = 1.25$. The arrows represent the velocity vectors. (a) $\gamma = 3.33$. (b) $\gamma = 5.60$. $R_{max} = 1.50$ mm.

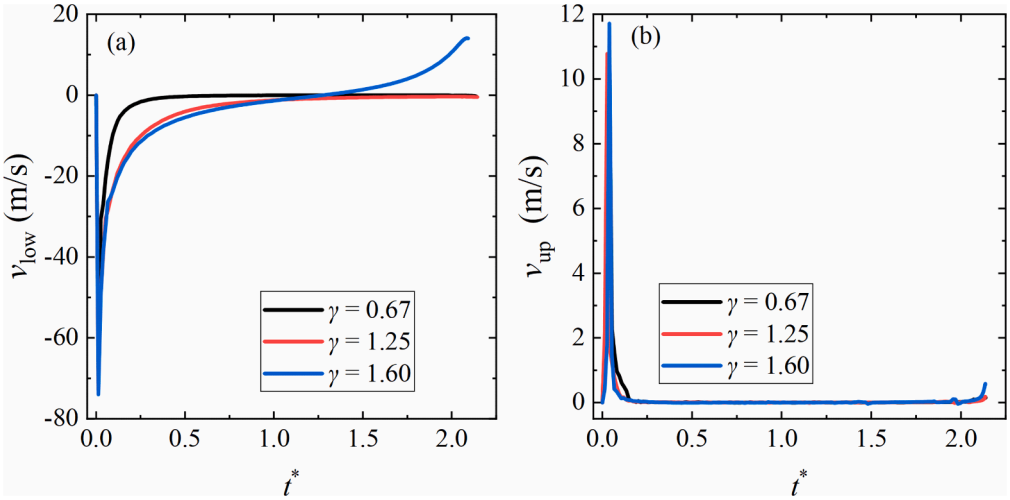


**Fig. 18.** Velocity variations of characteristic points on bubble interface for the case of bubble-splitting double jets. (a) Lowermost point of the bubble interface on *Y*-axis. (b) Uppermost point of the bubble interface on *Y*-axis. $\lambda = 0.16$ and $R_{max} = 1.50$ mm.

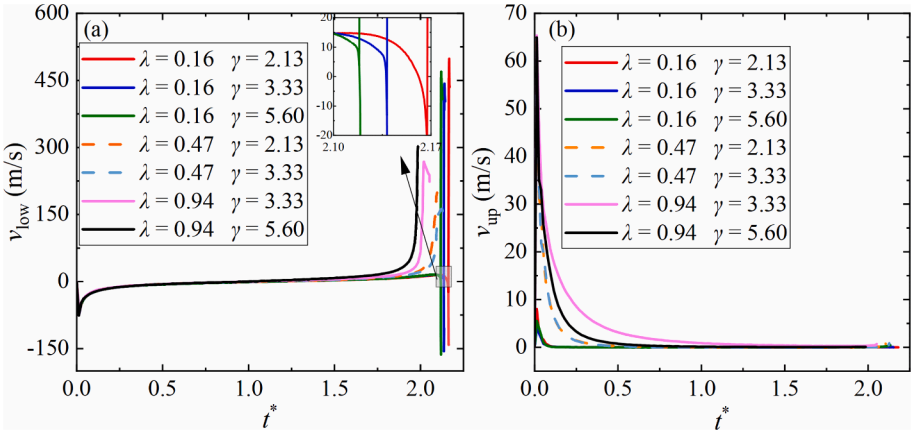


**Fig. 19.** Velocity variations of characteristic points on bubble interface for the case of impacting single jet. (a) Lowermost point of the bubble interface on *Y*-axis. (b) Uppermost point of the bubble interface on *Y*-axis. $R_{max} = 1.50$ mm.

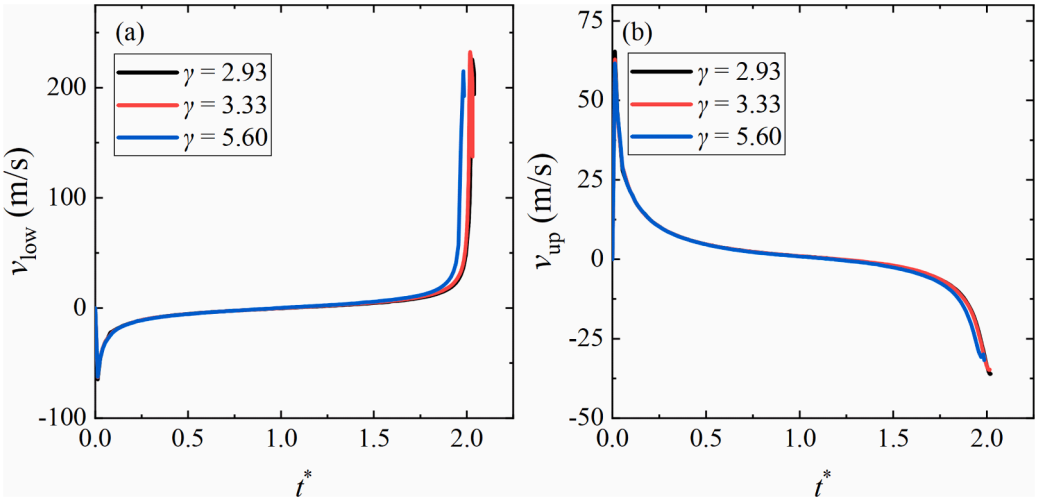


**Fig. 20.** Variations in jet velocity versus time for the case of non-impacting double jets. (a) Upward jet. (b) Downward jet. $\lambda = 1.25$ and $R_{max} = 1.50$ mm.

jet behaviour for $\lambda = 0.63$. From Fig. 16(a)–16(d), $\gamma$ gradually increases while the bubble–particle-1 distance $\lambda$ remains small. As $\gamma$ increases, the upper part of the bubble comes into contact with particle-1, suggesting that particle-1 exerts a more pronounced effect on the bubble. In frames 1–2 of Fig. 16(a), particle-2 flattens the lower interface of the bubble. From frames 3–4 in Fig. 16(a), the bubble breaks as its middle part

shrinks to the symmetry axis. Subsequently, two sub-bubbles each produce a jet. Compared with Fig. 15(a), the case illustrated in Fig. 16(a) produces double jets in opposite directions, but without the formation of two necks and their collisions. For larger particle spacings, i.e., Fig. 16 (b) and 16(c), the formation mechanism of jet remains consistent with that observed in Fig. 8. The differences lie in the bubble morphology and the jet shape during bubble collapse.

Fig. 17 shows the effect of the particle spacing parameter $\gamma$ on the jet behaviour for $\lambda = 1.25$. In these cases, the bubble is not contacting the two particles. Bubble proximity to particle-1 means that the downward jet is formed first [frame 3 in Fig. 17(a) and 17(b)]. Owing to the difference in liquid pressure above and below the bubble [frame 2 in Fig. 17(a) and 17(b)], the upward jet experiences a higher velocity compared to the downward jet [frame 4 in Fig. 17(a) and 17(b)].

## 7. Effect of bubble–particle distance on jet velocity

Fig. 18 demonstrates the velocity variations of characteristic points on bubble interface for the case of bubble-splitting double jets. The uppermost point and the lowermost point of the bubble interface on *Y*-axis are selected as interesting points. $v_{up}$ is the velocity at the uppermost point and $v_{low}$ is the velocity at the lowermost point. During the expansion stage of the bubble, its lower and upper interfaces move downward and upward, respectively. During the collapse stage of bubble, its upper and lower interfaces contact the particles, and their velocities remain unchanged. At small $\gamma$, i.e., $\gamma = 0.67$, the bubble maintains constant contact with both particles, and $v_{low}$ and $v_{up}$ are zero during the collapse stage. For large $\gamma$, i.e., $\gamma = 1.60$, the bubble does not contact particle-2 during the collapse stage. Therefore, the lower interface moves upward, and $v_{low}$ changes from negative to positive.

Fig. 19 demonstrates the velocity variations of characteristic points on bubble interface for the case of impacting single jet. In these cases, a single jet is produced below the bubble, and thus $v_{low}$ represents the jet velocity. For the bubble grows in Fig. 19(a), the lowermost point accelerates and then decelerates. During the collapse stage of bubble, for a long bubble–particle-1 distance (i.e., $\lambda = 0.47$ and 0.94), the jet velocity first rises slowly and then sharply. For a short bubble–particle-1 distance ($\lambda = 0.16$), a small sub-bubble detaches and collapses rapidly (see Fig. 11). As a result, $v_{low}$ exhibits a dramatic change for $t^* > 2.1$. Specifically, the positive values represent the jet velocity, and the negative values reflect the velocity of the small sub-bubble. For the small $\lambda$, the upper interface of the bubble consistently attaches to particle-1, and $v_{up}$ tends to be close to zero.

Fig. 20 illustrates the variations in jet velocity versus time for the case of non-impacting double jets. In these cases, the bubble forms double jets facing each other (see Fig. 13). Therefore, the velocity of the downward jet $v_{up}$ changes from positive (expansion stage) to negative (late collapse stage). The velocity of the upward jet $v_{low}$ follows a similar trend to the cases with $\lambda = 0.47$ and 0.94 in Fig. 19.

## 8. Conclusions

The current paper investigates the jet dynamics arising from a cavitation bubble in proximity to two particles, utilizing both experimental and numerical approaches. A high-speed camera captures the morphology changes of the laser-induced bubble, while numerical simulations accurately replicate the experimental findings and uncover the underlying jet evolution mechanism. The key findings are summarized as follows:

1. Depending on the mechanism of jet formation, the jet dynamics can be categorized into three cases. For the case of bubble-splitting double jets, the bubble has a short distance from both particles (dimensionless distance intervals of $\lambda < 1.0$ and $\gamma < 2.0$), thus bubble contraction at the top and bottom is inhibited by two particles. The bubble splitting produces double jets moving in opposite directions. For the case of impacting single jet, the bubble is close to one of the particles (dimensionless distance intervals of $\lambda < 1.0$ and $\gamma > 2.0$), its one side is inhibited by the particle, and the resulting jet direction is towards that particle. For the case of non-impacting double jets, the bubble has a long distance from the two particles (dimensionless distance intervals of $\lambda > 1.0$ and $\gamma > 2.0$), the bubble produces double jets facing each other.
2. The temperature variations inside the bubble during its collapse are related to the jet behavior. For the case of bubble-splitting double jets, the fluid near the bubble interface is at a low temperature and the center of the bubble is at a high temperature. For the case of impacting single jet, the fluid temperature is low near the jet and high near the particle. The temperature within the bubble reaches its peak upon jet penetration of the bubble interface. For the case of non-impacting double jets, the internal temperature of the bubble rises as the two jets approach.
3. The jet velocity depends on the formation mechanism, with jets arising from bubble splitting exhibiting a higher velocity compared to those resulting from bubble non-splitting.

## CRediT authorship contribution statement

**Yuning Zhang:** Writing – review & editing, Writing – original draft, Supervision, Funding acquisition, Conceptualization. **Xuan Lu:** Validation, Resources, Methodology. **Jinsen Hu:** Visualization, Software, Methodology, Formal analysis. **Jiaxin Yu:** Writing – review & editing, Project administration, Methodology, Formal analysis.

## Declaration of competing interest

The authors declare that they have no known competing financial interests or personal relationships that could have appeared to influence the work reported in this paper.

## Acknowledgement

The present research was funded by the National Natural Science Foundation of China (Project No. 52076215).

## References

[1] J. Sun, X. Ge, Y. Zhou, D. Liu, J. Liu, G. Li, Y. Zheng, Research on synergistic erosion by cavitation and sediment: a review, Ultrason. Sonochem. 95 (2023) 106399.
[2] C. Wang, Y.X. Zhang, H.C. Hou, J.Y. Zhang, C. Xu, Entropy production diagnostic analysis of energy consumption for cavitation flow in a two-stage LNG cryogenic submerged pump, Int. J. Heat Mass Transf. 129 (2019) 342–356.
[3] X. Wang, Q. Liang, Y. Yang, J. Shen, Z. Feng, Y. Zhang, Y. Zhang, Dynamics of single cavitation bubble collapse jet under particle-wall synergy, Phys. Fluids 36 (10) (2024) 103360.
[4] K. Kan, M. Binama, H.X. Chen, Y. Zheng, D.Q. Zhou, W.T. Su, A. Muhirwa, Pump as turbine cavitation performance for both conventional and reverse operating modes: a review, Renew. Sustain. Energy Rev. 168 (2022) 112786.
[5] J. Yu, X. Wang, J. Hu, J. Shen, X. Zhang, X. Zheng, Y. Zhang, Z. Yao, Laser-induced cavitation bubble near boundaries, J. Hydrodyn. 35 (2023) 858–875.
[6] Y. Zhang, F. Chen, Y. Zhang, Y. Zhang, X. Du, Experimental investigations of interactions between a laser-induced cavitation bubble and a spherical particle, Exp. Therm Fluid Sci. 98 (2018) 645–661.
[7] X. Wang, H. Su, S. Li, G. Wu, X. Zheng, Y. Duan, Y. Zhang, Experimental research of the cavitation bubble dynamics during the second oscillation period near a spherical particle, J. Hydrodyn. 35 (2023) 700–711.
[8] W. Xu, Y. Zhang, J. Luo, Q. Arong, Q. Zhang, Y. Zhai, The impact of particles on the collapse characteristics of cavitation bubbles, Ocean Eng. 131 (2017) 15–24.
[9] Y. Dai, H. Zhang, T. Chen, Influence of bubble–particle distance on the dynamic behaviors of a cavitation bubble near a particle, J. Hydrodyn. 35 (2023) 913–922.
[10] J. Zevnik, M. Dular, Cavitation bubble interaction with a rigid spherical particle on a microscale, Ultrason. Sonochem. 69 (2020) 105252.
[11] S. Li, R. Han, A.M. Zhang, Nonlinear interaction between a gas bubble and a suspended sphere, J. Fluids Struct. 65 (2016) 333–354.
[12] X. Wang, C. Zhang, H. Su, S. Li, J. Shen, Y. Zhang, J. Li, Y. Zhang, Research on cavitation bubble behaviors between a dual-particle pair, Phys. Fluids 36 (2) (2024) 023310.

[13] J.R. Blake, B.B. Taib, G. Doherty, Transient cavities near boundaries. Part 1. Rigid boundary, J. Fluid Mech. 170 (1986) 479–497.
[14] S. Li, A. Zhang, S. Wang, R. Han, Transient interaction between a particle and an attached bubble with an application to cavitation in silt-laden flow, Phys. Fluids 30 (2018) 082111.
[15] L. Zou, J. Luo, W. Xu, Y. Zhai, J. Li, Experimental study on influence of particle shape on shockwave from collapse of cavitation bubble, Ultrason. Sonochem. 101 (2023) 106693.
[16] S. Poulain, G. Guenoun, S. Gart, W. Crowe, S. Jung, Particle motion induced by bubble cavitation, Phys. Rev. Lett. 114 (21) (2015) 214501.
[17] S. Wu, Z. Zuo, H.A. Stone, S. Liu, Motion of a free-settling spherical particle driven by a laser-induced bubble, Phys. Rev. Lett. 19 (8) (2017) 084501.
[18] Y. Zheng, L. Chen, X. Liang, H. Duan, Numerical study of the interaction between a collapsing bubble and a movable particle in a free field, Water 12 (12) (2020) 3331.
[19] J. Wang, S. Li, J. Gu, A. Zhang, Particle propulsion from attached acoustic cavitation bubble under strong ultrasonic wave excitation, Phys. Fluids 35 (4) (2023) 042009.
[20] F. Xu, Y. Liu, M. Chen, J. Luo, L. Bai, Continuous motion of particles attached to cavitation bubbles, Ultrason. Sonochem. 107 (2024) 106888.
[21] X. Shen, R. Li, W. Han, S. Yang, H. Nan, L. Bai, Y. Dong, Dynamic characteristics of suspended particles influenced by cavitation bubble in a free field, Phys. Fluids 36 (8) (2024) 083313.
[22] D. Chen, M. Qiu, Z. Lin, Q. Liu, G. Zhang, Z. Zhu, Experimental study on the interaction of a cavitation bubble flanked by two particles, Acta Mech. 232 (2021) 4801–4810.
[23] X. Zheng, X. Wang, X. Lu, J. Yuan, Y. Zhang, Y. Zhang, Experimental research on the collapse dynamics of the cavitation bubble near two spherical particles, J. Mech. Sci. Technol. 37 (2023) 2451–2460.
[24] J. Hu, X. Lu, Y. Liu, J. Duan, Y. Lium, J. Yu, Numerical and experimental investigations on the jet and shock wave dynamics during the cavitation bubble collapsing near spherical particles based on OpenFOAM, Ultrason. Sonochem. 99 (2023) 106576.
[25] Z. Ren, Z. Zuo, S. Wu, S. Liu, Particulate projectiles driven by cavitation bubbles, Phys. Rev. Lett. 128 (4) (2022) 044501.
[26] F. Reuter, Q. Zeng, C.D. Ohl, The Rayleigh prolongation factor at small bubble to wall stand-off distances, J. Fluid Mech. 944 (2022) A11.
[27] C. Greenshields, OpenFOAM v10 User Guide, The OpenFOAM Foundation: London, UK, (2023).
[28] M. Koch, C. Lechner, F. Reuter, K. Köhler, R. Mettin, W. Lauterborn, Numerical modeling of laser generated cavitation bubbles with the finite volume and volume of fluid method, using OpenFOAM, Comput. Fluids 126 (2016) 71–90.
[29] L. Tian, Y.X. Zhang, J.Y. Yin, L. Lv, J.Y. Zhang, J.J. Zhu, Study on the liquid jet and shock wave produced by a near-wall cavitation bubble containing a small amount of non-condensable gas, Int. Commun. Heat Mass Transfer 145 (2023) 106815.
[30] K. Choi, S. Kim, H. Kim, C. Kim, Computational investigation on the non-isothermal phase change during cavitation bubble pulsations, Ocean Eng. 285 (2023) 115414.
[31] A.M. Zhang, S.M. Li, P. Cui, S. Li, Y.L. Liu, A unified theory for bubble dynamics, Phys. Fluids 35 (2023) 033323.
[32] J. Yu, J. Hu, Y. Liu, Y. Liu, D. Gao, Y. Zhang, Numerical investigations of the interactions between bubble induced shock waves and particle based on OpenFOAM, J. Hydrodyn. 36 (2024) 355–362.
[33] G. Xia, W. You, S. Manickam, J.Y. Yoon, X. Xuan, X. Sun, Numerical simulation of cavitation-vortex interaction mechanism in an advanced rotational hydrodynamic cavitation reactor, Ultrason. Sonochem. 105 (2024) 106849.
[34] A.M. Zhang, S. Li, J. Cu, Study on splitting of a toroidal bubble near a rigid boundary, Phys. Fluids 27 (6) (2015) 062102.
[35] L. Tian, Y. Zhang, J. Yin, L. Lv, J. Zhang, J. Zhu, Investigation on heat and mass transfer characteristics of a near-wall multi-cycle cavitation bubble and its thermal effects on the wall using an improved compressible multiphase model, Ocean Eng. 298 (2024) 117118.
[36] J.U. Brackbill, D.B. Koth, C. Zemach, A continuum method for modeling surface tension, J. Comput. Phys. 100 (2) (1992) 335–354.
[37] H.G. Weller, A new approach to VOF-based interface capturing methods for incompressible and compressible flow, OpenCFD Ltd., Report TR/HGW 4 (2008) 35.
[38] J. Yin, Y. Zhang, J. Zhu, L. Lv, L. Tian, An experimental and numerical study on the dynamical behaviors of the rebound cavitation bubble near the solid wall, Int. J. Heat Mass Transf. 177 (2021) 121525.
[39] B.R. Shin, Y. Iwata, T. Ikohagi, Numerical simulation of unsteady cavitating flows using a homogenous equilibrium model, Comput. Mech. 30 (2003) 388–395.
[40] Q. Zeng, H. An, C.D. Ohl, Wall shear stress from jetting cavitation bubbles: Influence of the stand-off distance and liquid viscosity, J. Fluid Mech. 932 (2022) A14.
[41] M. Koch, J.M. Rosselló, C. Lechner, W. Lauterborn, R. Mettin, Dynamics of a laser-induced bubble above the flat top of a solid cylinder—mushroom-shaped bubbles and the fast jet, Fluids 7 (1) (2021) 2.
[42] T.H. Phan, V.T. Nguyen, T.N. Duy, D.H. Kim, W.G. Park, Influence of phase-change on the collapse and rebound stages of a single spark-generated cavitation bubble, Int. J. Heat Mass Transf. 184 (2022) 122270.
[43] C. Lechner, W. Lauterborn, M. Koch, R. Mettin, Fast, thin jets from bubbles expanding and collapsing in extreme vicinity to a solid boundary: a numerical study, Phys. Rev. Fluids 4 (2) (2019) 021601.
[44] F. Reuter, C.D. Ohl, Supersonic needle-jet generation with single cavitation bubbles, Appl. Phys. Lett. 118 (13) (2021) 134103.